



Periodic orbits, pair nucleation, and unbinding of active nematic defects on conesFarzan Vafa ^{1,*}, David R. Nelson,² and Amin Doostmohammadi ³¹*Center of Mathematical Sciences and Applications, Harvard University, Cambridge, Massachusetts 02138, USA*²*Department of Physics, Harvard University, Cambridge, Massachusetts 02138, USA*³*Niels Bohr Institute, University of Copenhagen, Blegdamsvej 17, Copenhagen 2100, Denmark*

(Received 17 January 2024; accepted 6 May 2024; published 7 June 2024)

Geometric confinement and topological constraints present promising means of controlling active materials. By combining analytical arguments derived from the Born-Oppenheimer approximation with numerical simulations, we investigate the simultaneous impact of confinement together with curvature singularity by characterizing the dynamics of an active nematic on a cone. Here, the Born-Oppenheimer approximation means that textures can follow defect positions rapidly on the timescales of interest. Upon imposing strong anchoring boundary conditions at the base of a cone, we find a rich phase diagram of multidefect dynamics, including exotic periodic orbits of one or two $+1/2$ flank defects, depending on activity and nonquantized geometric charge at the cone apex. By characterizing the transitions between these ordered dynamical states, we present detailed understanding of (i) defect unbinding, (ii) defect absorption, and (iii) defect pair nucleation at the apex. Numerical simulations confirm theoretical predictions of not only the nature of the circular orbits but also defect unbinding from the apex.

DOI: [10.1103/PhysRevE.109.064606](https://doi.org/10.1103/PhysRevE.109.064606)**I. INTRODUCTION**

Nematic (apolar) order is ubiquitous in biological systems, ranging from subcellular filaments [1–3], to bacterial biofilms [4–6], and cell monolayers [7,8]. In two-dimensional nematics, which emerge when head-tail symmetry arises upon coarse-graining, the lowest energy defects are $\pm 1/2$ disclinations [9]. Notably, topological defects and their dynamics are often used to characterize *active* nematics, which consist of elongated units that consume energy to generate motion [10–12]. Moreover, these defects can mediate various biological functions, including cell extrusion and apoptosis in mammalian epithelia [13], neural mound formation [14], bacterial competition [15], and limb origination in simple animals such as regenerating *Hydra* [16]. For recent reviews on the significance of topological defects in biological systems, see Refs. [12,17,18].

The ability to control active materials, with their intricate interplay of topological defects, orientational order, flows, and geometry, would provide exciting new possibilities to transport matter, energy, and information far from equilibrium [10,19,20]. The control method we consider in this paper is confinement, which has been intensely studied in flat geometries such as channels [7,21–29], disks [23,29–35], and annuli [21,22,29,34,36–39]. Curved geometries have attracted less attention, with theoretical and experimental studies focusing on spherical [2,40,41], ellipsoidal [42,43], and toroidal [44,45] geometries. For a generic surface, Turner and Vitelli [46] showed that Gaussian curvature gives rise to an effective

topological charge density, which interacts with quantized topological defects.

However, these prototypical surfaces do not typically exhibit both nontrivial Gaussian curvature and a boundary that confines the nematic. The simplest geometry that embodies both properties is the cone, which is not only bounded by the base, but also flat everywhere except at the apex, where a delta function Gaussian curvature singularity resides. Moreover, in line with our previous work [47–49], since we can think of complex geometry as being composed of cones, then we expect that a cone qualitatively captures well a region of positive curvature. In the passive context, recent studies analytically determined the ground state defect configurations for liquid crystals on cones for free [47] and tangential [50] boundary conditions imposed at the base. With tangential boundary conditions, cone ground states for nematics can display two, one, or zero $+1/2$ defects on the flanks with increasing cone deficit angle [50]. Here, the cone deficit angle $2\pi\chi$ is given by the angular fraction χ of a flat disk removed to make a particular cone.

In this paper, we present dynamically ordered states of active topological defects on a cone. We extend our previous work [48] on the dynamics of a single active nematic defect near a curvature singularity to investigate the combined effect of strong anchoring boundary conditions at the cone base and apex curvature on the dynamic organization of active topological defects. By concentrating on regimes where activity allows one or two defects to survive on the cone flanks, we numerically uncover a rich phase diagram of periodic orbits of one or two $+1/2$ flank defects on a cone, with transitions between these states mediated by defect absorption, defect unbinding, or defect pair nucleation at the apex. Zero defect states on the cone flanks are also possible at high deficit

*Contact author: fvafa@cmsa.fas.harvard.edu

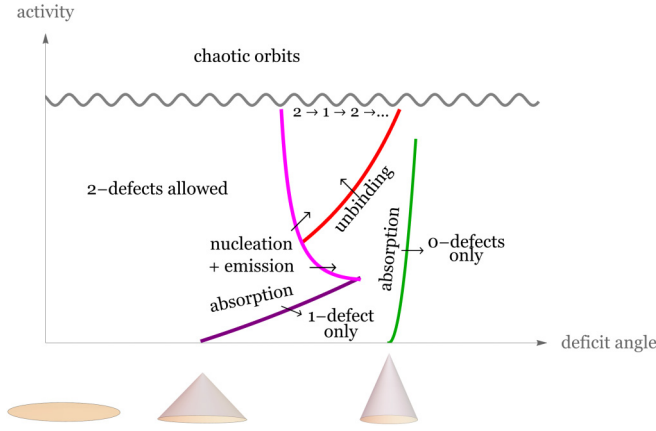


FIG. 1. Schematic phase diagram of main results. The colored curves guide the eye. At zero activity, the ground state consists of two flank defects (zero deficit angle, corresponding to a flat disk), one flank defect (deficit angle $2\pi\chi$ between 0 and $2\pi/3$, where the green curve intersects the x axis), and zero flank defects (deficit angle $2\pi\chi > 2\pi/3$) [50]. A more quantitative summary of our conclusions is represented in Fig. 5.

angles—see Fig. 1 for a summary of our main results, as a function of the cone deficit angle and activity. Moreover, we analytically explain many of the features of the phase diagram in Fig. 1.

This paper is organized as follows. We begin in Sec. II by briefly reviewing a minimal model of a general nematic texture in the one Frank constant approximation on an arbitrarily curved surface. By working deep in the ordered limit and utilizing isothermal coordinates (recently introduced in the context of liquid crystals [50,51], including those with a p -fold rotational symmetry), we construct and analyze in Sec. III the quasistatic multidefect solution in the passive setting on a curved surface. Our analysis reveals the presence of metastable states. Isothermal coordinates are particularly powerful for cones, with a delta function of Gaussian curvature, which acts like an unquantized defect charge. Activity enters in Sec. IV, where we review the Born-Oppenheimer approximation, which assumes textures rapidly adapt to defect motions, and its consequences, and also present details for the full numerical simulations for nematics on cones. In the following sections, we present our results in order of increasing activity, summarized schematically in Fig. 1. We begin by studying the dynamics of stable two $+1/2$ defect orbits and their polarizations in Sec. V. In Sec. VI, we turn to single-defect orbits and study the defect unbinding transition to two-defect stable orbits. Finally, in Sec. VII, we show that defect pair nucleation followed by emission from the cone apex is another mechanism for the $1 \rightarrow 2$ stable defect orbit transition, and for sufficiently large deficit angle, defect orbits cyclically transition between single- and two-defect orbits. Throughout the paper, we quantitatively test our theoretical predictions against full numerical simulations of overdamped active nematics on a cone, finding excellent agreement in the regime of low activity and for the location of various defect unbinding transitions. We also point out regimes where the physics is more challenging, such as the more chaotic defect dynamics that arise in our simulations for

large activity (see Fig. 1). Finally, in Sec. VIII, we summarize our main results and comment on potential experimental realizations of our predicted dynamically ordered defect structures, as well as on the relation to previous work and extensions.

II. MINIMAL MODEL IN ISOTHERMAL COORDINATES

We begin by briefly recalling the framework for describing a nematic texture on a curved surface, following the presentations in Refs. [50,51]. This review will then be followed by a description of the simulation methods. Throughout the paper we discuss theoretical predictions together with the results of full numerical simulations, testing our theoretical assumptions at each step.

A. Metric and nematic tensor

In two dimensions, it is always possible to choose local complex coordinates z and \bar{z} , known as isothermal (or conformal) coordinates, such that the square of the line element can be written as

$$ds^2 = g_{z\bar{z}}dzd\bar{z} + g_{\bar{z}z}d\bar{z}dz = 2g_{z\bar{z}}|dz|^2 = e^\varphi|dz|^2, \quad (1)$$

where e^φ is the conformal factor that describes position-dependent isotropic stretching or compression, and $g_{z\bar{z}} = e^\varphi/2$ is the metric [52].

In isothermal coordinates, the nematic order parameter \mathbf{Q} has only two nonzero components: $Q \equiv Q^{z\bar{z}}$ and $\bar{Q} \equiv Q^{\bar{z}z}$, with $Q = (\bar{Q})^*$. For ease of notation, let $\nabla \equiv \nabla_z$ and $\bar{\nabla} \equiv \nabla_{\bar{z}}$ denote the covariant derivatives with respect to z and \bar{z} , respectively. Covariant derivatives of \mathbf{Q} then simplify

$$\nabla Q = \partial Q + 2(\partial\varphi)Q, \quad \bar{\nabla} Q = \bar{\partial}Q, \quad (2a)$$

$$\bar{\nabla} \bar{Q} = \bar{\partial} \bar{Q} + 2(\bar{\partial}\varphi)\bar{Q}, \quad \nabla \bar{Q} = \partial \bar{Q}, \quad (2b)$$

where partial derivatives $\partial \equiv \partial/\partial z$ and $\bar{\partial} \equiv \partial/\partial \bar{z}$.

B. Conical geometry

In this paper, we focus on conical geometries. For a cone with half angle β , the metric can be obtained from $g_{z\bar{z}} = e^\varphi/2$ with

$$\varphi(z, \bar{z}) = -\chi \ln z\bar{z}, \quad (3)$$

where $\chi = 1 - \sin \beta$. The deficit angle of the cone is $2\pi\chi$, where χ represents the fraction of a disk missing when one unrolls the cone. This observation leads to another set of useful complex coordinates z' , which correspond to unrolling a cone to form a planar disk with a missing sector. The coordinates z' are related to z via the transformation

$$\bar{z}' = \frac{z^{1-\chi}}{1-\chi}, \quad (4)$$

where $\chi = 0$ represents a flat disk with no deficit angle. See Ref. [50] for more details and Fig. 2 for a schematic of these coordinate systems for a cone.

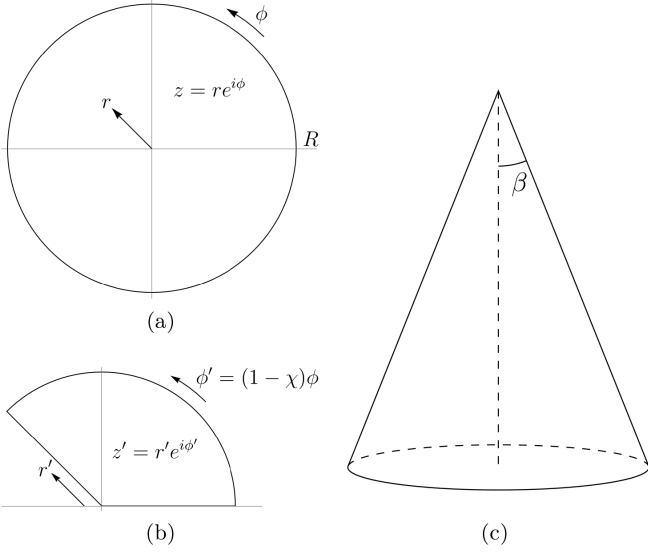


FIG. 2. Schematic of coordinate systems for a cone: (a) Isothermal coordinates $z = re^{i\phi}$. (b) Physical coordinates $z' = r'e^{i\phi'}$, corresponding to an unrolled cone with a missing sector, with angle fraction χ . If $0 \leq \phi \leq 2\pi$, then ϕ' ranges from 0 to $(1 - \chi)2\pi$. (c) A diagram of the cone in 3D with cone half angle β , where $\sin \beta = 1 - \chi$.

C. Free energy

The Landau-de Gennes free energy \mathcal{F} on a curved surface can be written as

$$\mathcal{F} = \int d^2z \sqrt{g} [K|\nabla Q|^2 + K'|\bar{\nabla} Q|^2 + \epsilon^{-2}(1 - S_0|Q|^2)^2], \quad (5)$$

where explicitly

$$|\nabla Q|^2 = g_{z\bar{z}} \nabla Q \bar{\nabla} \bar{Q}, \quad |\bar{\nabla} Q|^2 = g_{z\bar{z}} \bar{\nabla} Q \nabla \bar{Q} \quad (6)$$

$$|Q|^2 = g_{z\bar{z}}^2 Q \bar{Q}. \quad (7)$$

Here $K, K' > 0$ are Frank elastic type terms [53,54], and in regions of zero Gaussian curvature (such as any point on a cone other than the apex), the two terms are equivalent by integration by parts. The last polynomial term governs the isotropic-nematic transition, with ϵ controlling the microscopic coherence length and S_0 sets the equilibrium magnitude of the nematic order. We simplify by working in an approximation, which decouples the order parameter orientation from space, and thus makes no distinction between bend and splay deformations for $p = 2$ nematics. Without loss of generality we rescale the order parameter magnitude by setting $S_0 = 4$. Note that the cubic term that arises in 3D nematics is absent in two dimensions.

Deep in the ordered limit ($\epsilon \ll 1$), the free energy simplifies to [50]

$$\mathcal{F} = J \int d^2z |i\partial\alpha + \partial\varphi|^2, \quad (8)$$

where $J = K + K'$ and we have used $Q = e^{-\varphi} e^{i\alpha}$, where both φ and α can be functions of z and \bar{z} , with $\varphi(z, \bar{z})$ given by Eq. (3) for a cone.

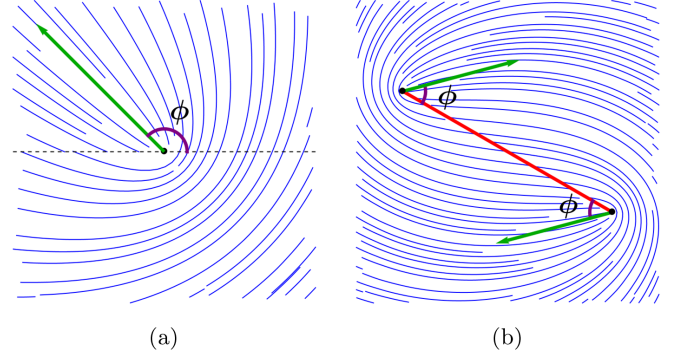


FIG. 3. Sketches of single-defect (a) and two-defect (b) nematic textures showing the polarization angle ϕ .

D. Multidefect solution

The multidefect ansatz Q_0 , given by

$$Q_0 = e^{2i\psi} e^{-\varphi} \prod_j \left(\frac{z - z_j}{|z - z_j|} \right)^{2\sigma_j}, \quad (9)$$

corresponds to minimizing \mathcal{F} [Eq. (8)], with fixed defect positions z_j of charges σ_j (we also include appropriate image charges to impose boundary conditions), and ψ is a constant global phase that defines the overall orientation of the nematic director [55] with respect to the base of the cone. Here the defect charges $\{\sigma_j\}$ for p -fold symmetric textures are integer multiples of $1/p$, where we focus in this paper on nematics with $\sigma_j = \pm 1/2$. Note that near a defect, e.g. $z \approx z_j$, the order parameter texture simplifies,

$$Q_0 \approx \left(\frac{z - z_j}{|z - z_j|} \right)^{2\sigma_j} e^{i\phi_j} e^{-\varphi}, \quad (10)$$

where the overall phase ϕ_j defines the polarization of the defect at z_j [55],

$$e^{i\phi_j} = e^{2i\psi} \prod_{j \neq i} \left(\frac{z_i - z_j}{|z_i - z_j|} \right)^{2\sigma_j}. \quad (11)$$

Defects do not have independent polarizations—the polarizations are uniquely determined by all of the defect positions and charges, as well as by ψ . See Fig. 3 for the polarizations associated with one- and two-defect textures. Note that for a $+1/2$ defect, ϕ_j is also the angle of the nematic director.

We now explicitly consider the case of two defects. From the structure of the polarization [Eq. (11)], it is easy to see that polarizations of neighboring defects are antiparallel [55,56]. For example, for the case of a pair of $+1/2$ defects and $\psi = \pi/4$, the defect polarizations are then perpendicular to the line connecting the two defects and point in opposite directions. See Fig. 3 for sketches of nematic textures for a single $+1/2$ defect and a pair of $+1/2$ defects that show the polarizations. We will return to this observation about the polarization when we consider the dynamics in Sec. IV, and then use full numerical simulations in Secs. V–VII to determine when the assumption of antiparallel polarizations is valid and when it breaks down.

E. Computation of the free energy

To compute the free energy, we must incorporate the boundary conditions. From here onwards, we consider the case of a nematic ($p = 2$) on a cone with strong anchoring boundary conditions at the base of radius R , by which we mean that the angle of the nematic director relative to the boundary is fixed [57]. To implement this boundary condition, for every defect j of charge $\sigma_j = \pm 1/2$ at z_j , we have a corresponding image defect of charge σ_j at $\bar{z}_j = R^2/\bar{z}_j$. Using a Gauss' law argument in two dimensions, one can show that the sum of the defect charges on the cone is 1 [50]. Upon recalling for a cone that $\varphi = -\chi \ln z\bar{z}$, computing the free energy [Eq. (8)] using the multidefect solution Q_0 [Eq. (9)] results in Ref. [50],

$$\mathcal{F} = -2\pi J \left\{ \sum_{m<n} \sigma_m \sigma_n \left[\ln \frac{|z_m - z_n|^2}{R^2} + \ln \left| 1 - \frac{z_m \bar{z}_n}{R^2} \right|^2 \right] + \sum_j \sigma_j^2 \ln \left(1 - \frac{|z_j|^2}{R^2} \right) - \chi \sum_j \left(\sigma_j - \frac{\sigma_j^2}{2} \right) \ln \frac{|z_j|^2}{R^2} \right\}, \quad (12)$$

where J plays the role of an elastic parameter in the one Frank constant approximation. The first term (the double sum) represents the elastic interaction between distinct defect pairs (including image charges). The second term is a position-dependent self-energy which would need to be added to any microscopic defect core energy E_c . Note that this position-dependent self-energy would vanish for a disk in the limit $R \rightarrow \infty$ for fixed $|z_j|$. The final term represents a Coulombic interaction between a topological defect and the geometry [46], specialized to the cone. The cone apex behaves as it develops an effective charge of $-\chi$, and that in interactions with the cone, the effective charge of the defect is modified from σ_j to $\sigma_j - \sigma_j^2/2$. Explicitly, for two defects, Eq. (12) becomes

$$\mathcal{F} = -2\pi J \left\{ \sigma_1 \sigma_2 \left[\ln \frac{|z_1 - z_2|^2}{R^2} + \ln \left| 1 - \frac{z_1 \bar{z}_2}{R^2} \right|^2 \right] + \sum_{j=1}^2 \sigma_j^2 \ln \left(1 - \frac{|z_j|^2}{R^2} \right) - \chi \sum_{j=1}^2 \left(\sigma_j - \frac{\sigma_j^2}{2} \right) \ln \frac{|z_j|^2}{R^2} \right\}, \quad (13)$$

where for nematics we will typically set $\sigma_j = \pm 1/2$.

F. Forces

Having computed the free energy, we can now compute from Eq. (12) the \bar{z} component of the force on defect i , i.e., $F_i^{\bar{z}} = -\frac{\partial \mathcal{F}}{\partial \bar{z}_i}$, which is given by

$$F_i^{\bar{z}} = -2\pi J \left\{ \sigma_i \sum_{j \neq i} \sigma_j \left[\frac{1}{z_i - z_j} + \frac{1}{z_i - \bar{z}_j} \right] + \sigma_i^2 \frac{1}{z_i - \bar{z}_i} - \chi \left(\sigma_i - \frac{\sigma_i^2}{2} \right) \frac{1}{z_i} \right\}$$

$$= -2\pi J \left\{ \sigma_i \sum_{j \neq i} \sigma_j \frac{1}{z_i - z_j} + \sigma_i \sum_j \sigma_j \frac{1}{z_i - \bar{z}_j} - \chi \left(\sigma_i - \frac{\sigma_i^2}{2} \right) \frac{1}{z_i} \sum_{j \neq i} \right\}, \quad (14)$$

where we remind the reader that \bar{z}_j gives the position of a like-signed image charge, $\bar{z}_j = R^2/\bar{z}_j$. All three terms represent Coulomb forces: the first term, the forces from other defects on the cone flanks; the second term, the forces due to all of the image charges; the third term, a force due to the apex. Explicitly, for two defects, the force on defect 1 from all these sources is

$$F_1^{\bar{z}} = -2\pi J \left[\sigma_1 \sigma_2 \frac{1}{z_1 - z_2} + \sigma_1^2 \frac{1}{z_1 - \bar{z}_1} + \sigma_1 \sigma_2 \frac{1}{z_1 - \bar{z}_2} - \chi \left(\sigma_1 - \frac{\sigma_1^2}{2} \right) \frac{1}{z_1} \right]. \quad (15)$$

III. STATIONARY SOLUTIONS IN PASSIVE CASE ON A CONE

A. Stability for two defects

We know that for a passive nematic texture on a cone with $0 < \chi < 2/3$, there exists a stable solution where one $+1/2$ defect is at the apex and the other is on the flanks [50]. However, for the case of nematic texture on a disk ($\chi = 0$), a stable solution is two antipodal $+1/2$ defects [30,50], in agreement with experiments of fibroblasts on disks [30]. Thus it is clear that starting from this solution, for sufficiently small χ , by continuity there should exist a locally stable solution of two antipodal $+1/2$ defects, even though it may not be a global energetic minimum. We now explicitly show this by considering the 4×4 Hessian $H_{ij} = \frac{\partial}{\partial x_i} \frac{\partial}{\partial x_j} \mathcal{F}$ of Eq. (12), where $i, j = 1, \dots, 4$ and $z_1 = x_1 + ix_2$ and $z_2 = x_3 + ix_4$. By evaluating the eigenvalues of H_{ij} at the antipodal extremum, specifically at $z_1 = x_c$, $z_2 = -x_c$, where $x_c = (\frac{1-3\chi}{5-3\chi})^{1/4} R$ for a pair of $+1/2$ defects, we find that x_c is a local minimum for $0 < \chi < 1 - \frac{1}{3}\sqrt{5 - \frac{1}{\sqrt{2}}} = 0.31$. We thus learn that on a cone, there are two locally stable stationary solutions for small enough χ : one solution has one $+1/2$ defect at the apex with another $+1/2$ defect on the flanks, while the second solution has two $+1/2$ defects on the flanks. The global minimum of \mathcal{F} is obtained for the former. See Fig. 4 for a plot of the potential [Eq. (12)] for a pair of $+1/2$ defects that graphically demonstrates that the two flanks defect configuration is a local but not global minimum. Although more generally, two antipodal flank defects can be written as $z_1 = e^{i\phi} x_c$, $z_2 = e^{i(\phi+\pi)} x_c = -e^{i\phi} x_c$, rotational invariance insures that the energy is independent of ϕ . Note that when χ is nonzero, a flank distance x_c in isothermal coordinates because a physical distance $x'_c = x_c^{1-\chi}/(1-\chi)$, measured from the apex of the cone [see Eq. (4)].

IV. DYNAMICAL EQUATION

The minimal model presented thus far describes statics of passive nematic defects on curved geometries. We now

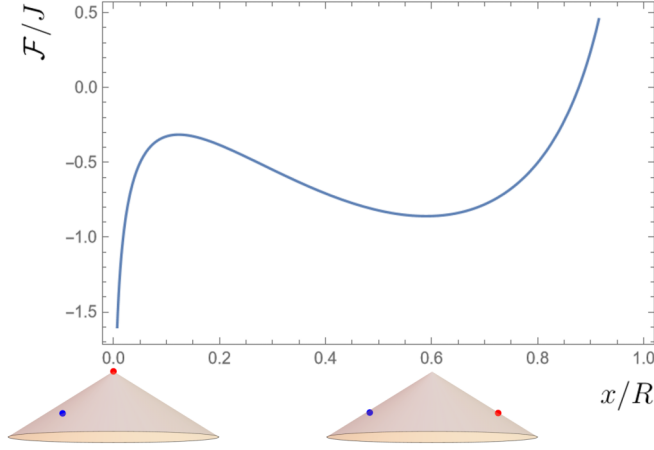


FIG. 4. Plot of potential [Eq. (13)] for $\chi = 0.15$ for a pair of $+1/2$ defects, where one defect is at $x_c = -0.59R$ and the other is at an arbitrary (antipodal) flank position x . The local minimum is at $x = x_c$, but it's not the global minimum as $x \rightarrow 0$. Cones below the x axis indicate the solutions at the extrema, where the colored dots indicate the two $+1/2$ defects. Here $|x_c| \approx 0.59R$ is the position found in Ref. [50] for the ground state with a single defect on the flank for $\chi = 0.15$.

introduce a simple overdamped model for the dynamics of the defects, explicitly accounting for the effect of active stress generation by the nematogens.

We assume that the motion of the nematic order parameter is controlled by the balance of relaxational dynamics and advection of the tensorial order parameter by a velocity flow field v , according to

$$\gamma D_t Q = -\frac{1}{\sqrt{g}} g^{z\bar{z}} g^{z\bar{z}} \frac{\delta \mathcal{F}}{\delta \bar{Q}}, \quad (16)$$

where

$$D_t Q = \partial_t Q + (v \nabla + \bar{v} \bar{\nabla}) Q - (\nabla v - \bar{\nabla} \bar{v}) Q \quad (17)$$

is the generalized advective time derivative of Q , accounting for both regular advection by the flow and reorientation response to flow gradients [48,58] and

$$\begin{aligned} & -\frac{1}{\sqrt{g}} g^{z\bar{z}} g^{z\bar{z}} \frac{\delta \mathcal{F}}{\delta \bar{Q}} \\ & = g^{z\bar{z}} (K \nabla \bar{\nabla} + K' \bar{\nabla} \nabla) Q + 2\epsilon^{-2} S_0 (1 - S_0 |Q|^2) Q \\ & = J g^{z\bar{z}} (\partial \bar{\partial} Q + 2\partial \varphi \bar{\partial} Q) + 2\epsilon^{-2} S_0 (1 - S_0 |Q|^2) Q \end{aligned} \quad (18)$$

is the molecular field, which tries to minimize the energy in the absence of active forces. In the second line is the explicit expression for the case of a conical geometry.

Upon assuming that the flow is generated by active stresses and working in the overdamped limit [59–62], the balance of the active force and the frictional damping leads to

$$\mu v = \zeta_Q \nabla Q, \quad (19)$$

where μ is a friction coefficient and ζ_Q is the scalar activity that characterizes the strength of the active stress. We can thus write

$$v = \frac{\zeta_Q}{\mu} \nabla Q = \zeta \nabla Q = \zeta (\partial \varphi + i \partial \alpha) Q,$$

where $\zeta = \zeta_Q / \mu$ and we have used Eq. (2a) and $Q(z, \bar{z}) = e^{-\varphi} e^{i\alpha}$.

A. Born-Oppenheimer approximation

Since the multidefect ansatz is a stationary solution in the passive setting, then we expect that for small activity, the multidefect ansatz is still a good solution, provided that the defects are allowed to move, but slowly. Explicitly, we now assume

$$Q_0 = e^{2i\psi} e^{-\varphi} \prod_j \left(\frac{z - z_j(t)}{|z - z_j(t)|} \right)^{2\sigma_j}, \quad (20)$$

so that the nematic texture rapidly readjusts itself in response to the slow motion of the defects. This is known as the Born-Oppenheimer approximation when studying the quantum mechanics of light-weight electrons bonding atoms with much heavier nuclei [63].

B. Forces and polarization for a pair of $+1/2$ defects

We now consider the implications of the Born-Oppenheimer approximation for the two-defect arrangement on a cone that is the prime focus in this paper. Within the Born-Oppenheimer approximation, the Coulombic forces on a pair of defects [Eq. (15) derived in Sec. II] are still correct, and the motile force on a $+1/2$ defect j is given by [55]

$$F^M = e^{2i\psi} \frac{\pi}{4} \frac{1}{a} \zeta. \quad (21)$$

Thus, a $+1/2$ defect travels at constant speed along its axis $e^{i\psi}$ (with opposite sign for the other defect, since for two defects, $e^{i\phi_j} = \pm e^{i\psi}$). The motile force F^M has magnitude $\frac{\pi}{4} \frac{\zeta}{a}$ and makes an angle ψ relative to the line connecting the defect to the apex (the radial line). Specifically, we can decompose F^M into radial F_r^M and tangential F_θ^M components as

$$F_r^M = \frac{\pi}{4} \frac{\zeta}{a} \cos 2\psi, \quad (22a)$$

$$F_\theta^M = \frac{\pi}{4} \frac{\zeta}{a} \sin 2\psi. \quad (22b)$$

Explicitly, for an active $+1/2$ defect labeled 1 in the presence of another $+1/2$ defect labeled 2, the force on defect 1 is

$$\begin{aligned} F_1^{\bar{z}} = & -\frac{\pi J \gamma^{-1}}{2} \left[\frac{1}{z_1 - z_2} + \frac{1}{z_1 - \bar{z}_1} + \frac{1}{z_1 - \bar{z}_2} - \frac{3}{2} \chi \frac{1}{z_1} \right] \\ & + e^{i\psi} \frac{\pi}{4} \frac{\zeta}{a}. \end{aligned} \quad (23)$$

In addition to the forces on defects, the Born-Oppenheimer approximation implies for a pair of neighboring defects that

- (1) the polarizations are antiparallel [55,56], and
- (2) the polarization relative to the line connecting the two defects does not change in time,

even as the defects move [64]. Inspired by these theoretical considerations, we now assess the validity of the Born-Oppenheimer approximation by directing comparing theoretical predictions with full numerical simulations.

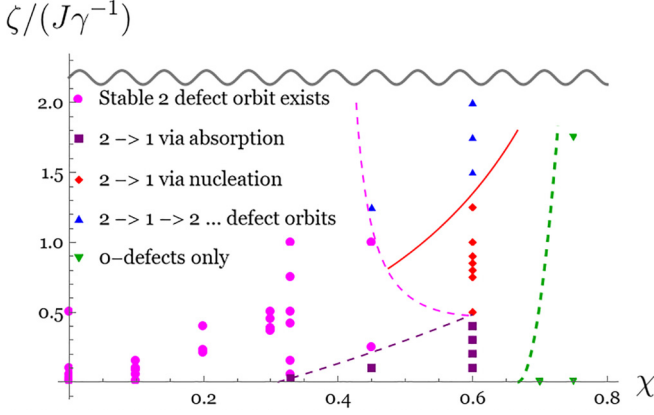


FIG. 5. Phase diagram of main results with data from simulations included. The colored dashed curves, based on the data, guide the eye. The solid red curve is given by Eq. (30) with $c' = 0.9$. We have not explored the regime above the wavy horizontal line, which exhibits more chaotic dynamics.

C. Simulation details

We check our theory with numerical simulations of the full active nematic texture on a cone, according to Eqs. (16)–(18). Without loss of generality, since a cone has zero Gaussian curvature everywhere except at the apex, we set $K' = 0$ in the simulations. We impose strong anchoring boundary conditions at the base, i.e., the nematic director is at a fixed angle relative to the boundary. Explicitly, we impose at the boundary of the cone base of radius R in the isothermal coordinate of Fig. 2(a), i.e., at $z = Re^{i\phi}$ where ϕ is the azimuthal coordinate):

$$Q = e^{2i\psi} e^{-\varphi+i\phi}. \quad (24)$$

Here, ψ specifies the nematogen orientation at the boundary. We shall often do simulations with $\psi = \pi/4$, which leads to especially interesting dynamics. In our simulations, we solve Eqs. (16)–(18) numerically using the method of lines [65], where the temporal evolution is performed through a predictor-corrector scheme [66] and spatial derivatives are evaluated using five-point stencil central differences. The phase diagram of our main results, which will be the central focus of the remainder of our paper, can be seen in Fig. 5.

V. STABLE TWO-DEFECT ORBITS FOR $0 \leq \chi < 0.31$

We start with small activity on a disk and then extend to a cone by incrementally increasing the deficit angle $2\pi\chi$. We analyze two different setups in order: (1) two flank defects and then (2) one defect at the apex and the other on the flanks.

A. Two-defect orbits on a disk ($\chi = 0$)

As discussed previously in Sec. III, we know for a passive nematic on a disk that there is a stable two flank defect configuration [30,50,67,68]. Thus, it is reasonable to expect that for small activity there should still be a stable two flank defect configuration, where now the defects can possibly move. We now show that there are indeed stable circular orbits on a disk.

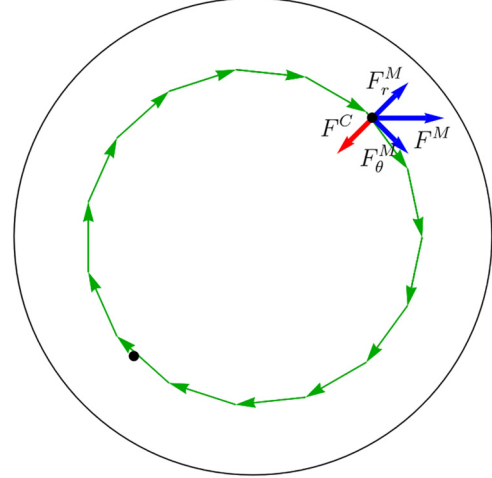


FIG. 6. Sketch of forces for a pair of $+1/2$ defects on a disk ($\chi = 0$). The net Coulomb repulsion F^C is in red, the motile force F^M , decomposed into its radial F_r^M and tangential F_θ^M components, is in blue, and the defects follow the green arrows to form a circle.

We simulate an active nematic on a disk and we consider three cases: $\psi = 0, \pi/8, \pi/4$. In all three cases, in the simulations the distance of the defect to the center was constant. We now argue that this behavior follows from the Born-Oppenheimer approximation for both disks and cones.

If at the boundary the phase is $\psi = 0$, then since the motile force is radial, and the Coulomb force is always radial, activity simply shifts the equilibrium position, and hence we would still have static solution in this case. If, however, the phase is $\psi = \pi/4$, since the motile force is perpendicular to the radial line, (and remains perpendicular as the defect moves as explained in the previous section), the distance from the apex does not change, and the defect moves in a circular orbit (see Fig. 7). For a more generic phase ψ , the radial distance readjusts so that the net Coulomb force (including any contribution from the cone apex) balances the radial component of the motile force; the remaining tangential component of the motile force causes the flank defects to undergo circular motion. Note that the sense of rotation (clockwise in Fig. 7) is determined by the initial polarizations.

Explicitly, we now solve for the distance r by setting the radial component of the net force given in Eq. (23) to zero. Since for a disk $\chi = 0$, we find from Eq. (23) that

$$\frac{\pi J \gamma^{-1}}{2} \left[\frac{1}{2r} + \frac{1}{R^2/r + r} - \frac{1}{R^2/r - r} \right] = \frac{\pi \zeta}{4a} \cos 2\psi. \quad (25)$$

Note the contributions from the image defects to the force inside the square brackets. See Fig. 6 for a sketch. We thus conclude that generically defects will have circular orbits with constant speed due to vanishing net radial force and nonzero azimuthal component of the motile force. We want to emphasize that there is no centripetal force, since the net radial force vanishes.

For $\psi = 0$, as expected, there was no orbital motion, since the motility has no tangential component. For $\psi = \pi/8, \pi/4$, defects formed circular orbits (see Fig. 7 for representative snapshots of stable circular orbits of two defects on a disk for

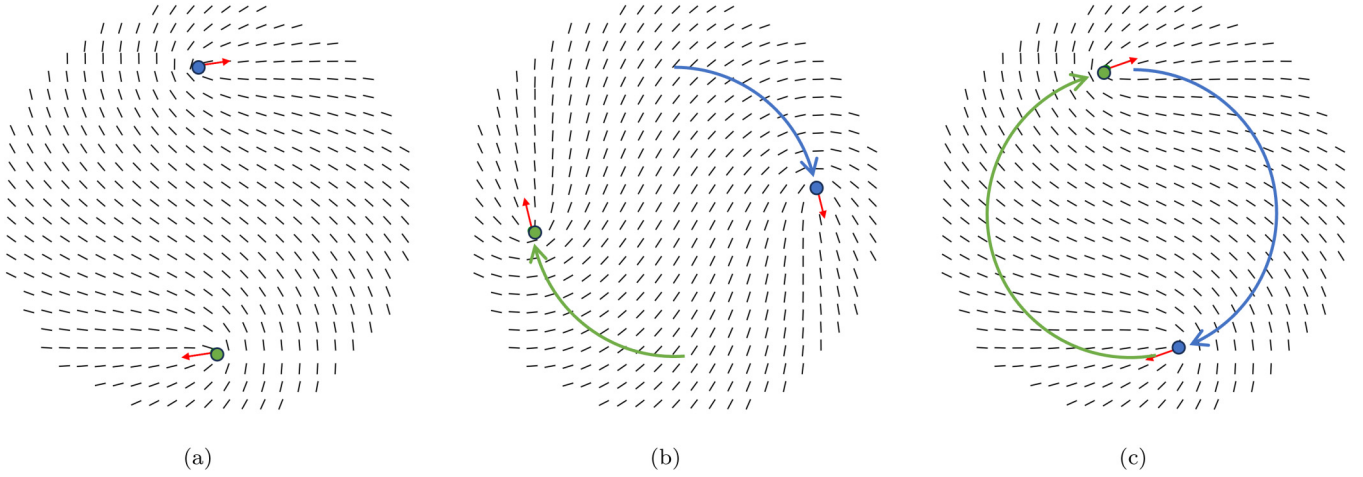


FIG. 7. Representative sequential snapshots of simulations on a disk for $\zeta/(J\gamma^{-1}) = 0.01$ and $\psi = \pi/4$. In all of the plots, the colored dots denote the $+1/2$ defects which follow the corresponding colored trajectories, and the red arrows denote the polarizations of the $+1/2$ defects. The activity parameter chosen here leads to motion in the direction of the red polarization arrows.

$\psi = \pi/4$). For all three values of ψ , the radial components of the defects, with defect core size $a = 0.9$, were as expected from Eq. (25). Moreover, upon inserting the mobility matrix from Ref. [55] into the dynamical equations,

$$\mathcal{M}_{ii}\dot{z}_i = -\frac{\pi J\gamma^{-1}}{2} \left[\frac{1}{2r} + \frac{1}{R^2/r+r} - \frac{1}{R^2/r-r} \right] + \frac{\pi \zeta}{4a} \cos 2\psi, \quad (26)$$

we can estimate the speed of the defects, where the mobility \mathcal{M}_{ii} is a complicated function of the defect positions and the disk size R ,

$$\mathcal{M}_{ii} = \frac{\pi}{2} \sigma_i^2 \left\{ \ln \left(\frac{R^2 - r_i^2}{a^2} \right) - \frac{R^2 - 2r_i^2}{R^2 - r_i^2} + \frac{R^4 \left[r_i^2 (3r_i^2 - 2R^2) - 2(R^2 - r_i^2)^2 \ln \left(1 - \frac{r_i^2}{R^2} \right) \right]}{2r_i^6 (r_i^2 - R^2)} \right\}. \quad (27)$$

The theoretical prediction for the speed following from Eqs. (26) and (27) was confirmed by the simulations to within about 4%, which is surprisingly good agreement given that we know that the Born-Oppenheimer ansatz of Eq. (9) is not exact. Assuming for simplicity the mobility is independent of the defect position, we find theoretically that the ratio of speeds for $\psi = \pi/4$ and $\psi = \pi/8$ is $\sqrt{2} \approx 1.4$, which is close to the numerical value of $2.8/1.9 \approx 1.5$. In Table I, we provide a quantitative comparison between the numerical results and theoretical predictions by including the mobility,

showing good agreement and verifying the validity of our Born-Oppenheimer approximation for the parameter values used in our disk simulations.

B. Two metastable defect orbits on cone with $0 < \chi < 0.31$

Having verified the dynamics against full simulations on a disk, we now begin with extending our analyses to the cone, incrementally increasing the deficit angle $2\pi\chi$ upwards from zero. For $\zeta = 0$ (i.e., with no activity) and $\chi < 0.31$, we know that there is a locally stable two flank defect configuration, even though the true ground state has a single flank defect with the other defect at the apex. For small deficit angles, similar to the case of a disk, it is reasonable to expect that for small activity there should still be a locally stable two flank defect configuration, where the defects can possibly move. We now show that for small activity there are stable circular orbits on a cone for $\chi < 0.31$, with a radius that depends on the activity.

We solve for the orbital radius r by again setting the radial component of the net force given in Eq. (23) to zero, leading to

$$\frac{\pi J\gamma^{-1}}{2} \left[-\frac{3}{2} \frac{\chi}{1-\chi} \frac{1}{r} + \frac{1}{2r} + \frac{1}{R^2/r+r} - \frac{1}{R^2/r-r} \right] = \frac{\pi \zeta}{4a} \cos 2\psi. \quad (28)$$

See Fig. 8 for a sketch of the forces acting on the flank defects. As before, since the radial component of the motile force, if any, balances the net Coulomb force, and the tangential component of the motile force is constant, then defects

TABLE I. Table of defect distances from the cone apex in isothermal coordinates and speeds for $\zeta/(J\gamma^{-1}) = 0.01$ and $\psi = 0, \pi/8, \pi/4$ for both theoretical prediction and simulation result on a disk. Here the short distance cutoff $a = 0.9$.

Phase ψ	Theoretical distance	Numerical distance	Theoretical speed (ζ/a)	Numerical speed (ζ/a)
0	$0.76R$	$0.76R$	0	0
$\pi/8$	$0.75R$	$0.75R$	1.9×10^{-4}	1.9×10^{-4}
$\pi/4$	$0.68R$	$0.68R$	2.7×10^{-4}	2.8×10^{-4}

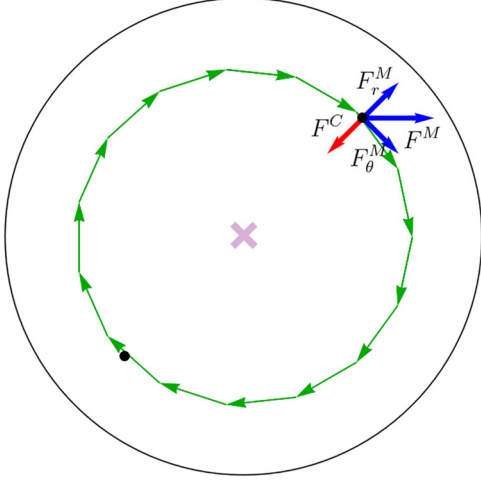


FIG. 8. Sketch of forces for a pair of $+1/2$ defects on a cone. Black dots denote $+1/2$ defects and purple star denotes apex. Net Coulomb repulsion F^C is in red, the motile force F^M , decomposed into its radial F_r^M and tangential F_θ^M components, is in blue, and the defects follow the green arrows.

will typically have circular orbits with constant speed, with a χ -dependent radius. The behavior is thus qualitatively independent of χ . See Table II for comparison of theory to simulations for nearly flat cones with $\chi = 1/10$, $\frac{\zeta}{J\gamma^{-1}} = 0.01$, and $\psi = 0, \pi/8, \pi/4$.

VI. SINGLE-DEFECT ORBITS AND DEFECT UNBINDING ON A CONE

As shown in Sec. III and Ref. [50] for a passive nematic texture on a cone, the global minimum of the configuration is a single $+1/2$ defect on the cone flank. This ground state provides a natural starting point to investigate basic features of an isolated $+1/2$ defect on a flank and its active dynamics.

A. Single-defect orbits

We start with the single flank defect ground state solution obtained in Ref. [50], which is valid for $\chi < 2/3$. We now add small activity.

As usual, we solve for the distance r of the isolated flank defect from the apex in isothermal coordinates by setting the radial component of the net force given in Eq. (23) to zero,

TABLE II. Table of defect distances from the cone apex in isothermal coordinates for $\chi = 1/10$ and $\zeta/(J\gamma^{-1}) = 0.01$ for $\psi = 0, \pi/8, \pi/4$ for both theoretical prediction and simulation results. Here $a = 0.9$.

Phase ψ	Theoretical distance	Numerical distance
0	$0.70R$	$0.70R$
$\pi/8$	$0.68R$	$0.69R$
$\pi/4$	$0.62R$	$0.63R$

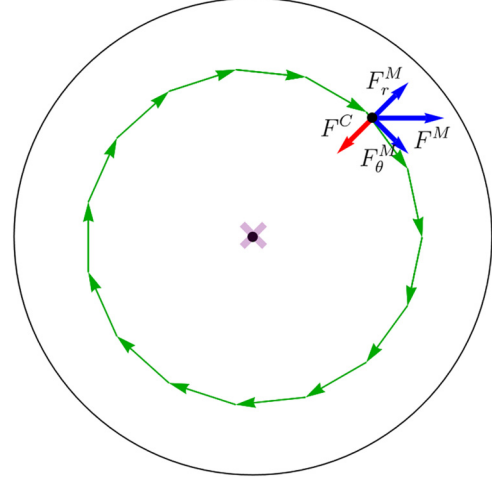


FIG. 9. Sketch of forces for a pair of $+1/2$ defects on a cone, where one defect is at the apex and the other is on the flanks. Black dots denote $+1/2$ defects and purple star denotes the apex, which has an effective negative topological charge that interacts with the orbiting defect. Net Coulomb repulsion F^C is in red, the motile force F^M , decomposed into its radial F_r^M and tangential F_θ^M components, is in blue, and the flank defect follows the green arrows.

leading to

$$\frac{\pi J\gamma^{-1}}{2} \left[-\frac{3}{2} \frac{\chi}{1-\chi} \frac{1}{r} + \frac{1}{r} - \frac{1}{R^2/r-r} \right] = \frac{\pi \zeta}{4a} \cos 2\psi. \quad (29)$$

See Fig. 9 for a sketch of the forces acting on a single flank defect. Similar to the two-defect case, the defect will circularly orbit the apex at constant speed, which is not driven by a centripetal force, since the net radial force vanishes.

For comparison of the Born-Oppenheimer dynamical theory to numerics, see Table III for $\chi = 1/10$, $\frac{\zeta}{J\gamma^{-1}} = 0.01$, and $\psi = \pi/8, \pi/4$, and Table IV for $\chi = 1/3$, $\frac{\zeta}{J\gamma^{-1}} = 0.25$, and $\psi = 0, \pi/4$. These tables suggest that for small χ and ζ , the multidefect ansatz is good, but becomes worse as χ and ζ increase for nonzero ψ . We observed in the simulations that the polarizations of the defects rotated to point outwards, consistent with the observation that the numerical distance is larger than the prediction in Table IV. This discrepancy suggests that the global phase ψ becomes space-dependent as χ and ζ increase, which is not captured in our ansatz.

TABLE III. Table of defect distances from the cone apex in isothermal coordinates for $\chi = 0.1$ and $\zeta/(J\gamma^{-1}) = 0.01$ for $\psi = \pi/8, \pi/4$ for both theoretical prediction and simulation result on a cone. Here $a = 0.9$.

Phase ψ	Theoretical distance	Numerical distance
$\pi/8$	$0.72R$	$0.73R$
$\pi/4$	$0.71R$	$0.69R$

TABLE IV. Table of distances for $\chi = 1/3$ and $\zeta/(J\gamma^{-1}) = 0.25$ for $\psi = 0, \pi/4$ for both theoretical prediction and simulation result on a cone. Here $a = 0.9$.

Phase ψ	Theoretical distance	Numerical distance
0	0.88R	0.87R
$\pi/4$	0.58R	0.78R

B. 1 \rightarrow 2 defect transition via defect unbinding

Numerical simulations allow us to explore a larger phase space of stronger activities. Upon initializing with the zero activity ground state, for a small activity, we observed one defect at the apex and a single-defect orbit on the cone flank, and for sufficiently large activity, the $+1/2$ defect at the apex experiences a stronger motile force, which can be sufficient to allow the defect to escape the Coulombic attraction to the apex due to the deficit angle, i.e., due to a nonzero χ . As the defect unbinds from the apex, the defects on the flanks can experience circular motion equidistant from the apex as before (see Fig. 10 for key snapshots depicting the unbinding mechanism for $\psi = \pi/4$.)

We estimate the critical value for the activity ζ_c by equating the motile force with the Coulomb force at the apex in physical coordinates [48]:

$$3c \frac{\chi}{1-\chi} \frac{J\gamma^{-1}}{a} = \frac{\zeta_c}{a} \Rightarrow \zeta_c = c' J\gamma^{-1} \frac{\chi}{1-\chi}, \quad (30)$$

where $c' = 3c$. We introduced an adjustable factor of c in the LHS to model the defect core size $\sim a$, and from simulations learn that $c' = 3c \approx 0.9$. Comparison of this analytically calculated critical activity threshold for defect unbinding with the results of full numerical simulations shows good agreement, with a single adjustable parameter (see Fig. 11). As such, we argue that for any experimental realization of an overdamped active nematic layer on a cone, using Eq. (30), and knowing the material constants of the nematic texture, i.e., the Frank elasticity J and orientational diffusion constant γ , the critical activity for the unbinding of nematic topological defects can be found for any conical geometry with deficit angle $2\pi\chi$.

VII. LARGE DEFICIT ANGLE AND ACTIVITY

A. Stable two-defect configurations for $\chi > 0.31$

For $\chi > 0.31$ and sufficiently small activity, we expect there to be no stable two flank defect configuration. Indeed, the ground state for $\zeta = 0$ contains only 1 flank defect for $0 < \chi < 2/3$ and 0 flank defects for $2/3 < \chi < 1$ [50]. Hence, if we start with two flank defects, then we expect that the dynamics will lead to 1 flank defect, with the other defect absorbed by the apex. Consistent with our analysis of defect absorption by the apex in Ref. [48], our simulations do indeed reveal see defect absorption in this regime.

However, from simulations we learn that sufficiently large activity can in fact stabilize the two-defect orbit for $\chi = 1/3$, even though the ground state for $\zeta = 0$ has only a single defect

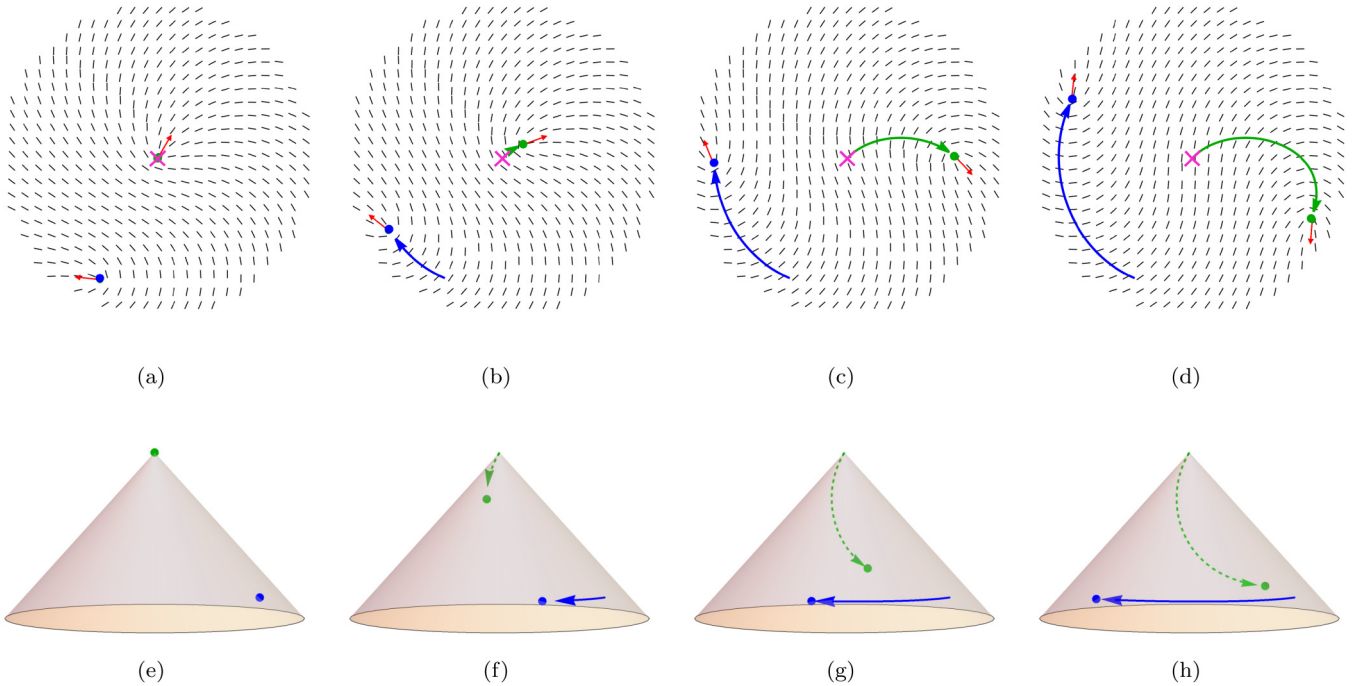


FIG. 10. Key snapshots of simulations showing how a defect unbinds from the apex in the presence of activity. Top row: plots are in isothermal coordinates on a cone with $\chi = 0.33$ and $\zeta/(J\gamma^{-1}) = 0.5$ and $\psi = \pi/4$. (a) Initially a single defect is orbiting. (b) The $+1/2$ defect begins unbinding from the apex. (c) The $+1/2$ defect has successfully unbound (escaped) from the apex. (d) Representative snapshot of stable circular two-defect orbit. The bottom row shows a perspective view of the cone itself. The dashed green line shows that a trajectory initially lies on the far side of the cone. In all of the plots, the colored dots denote the $+1/2$ defects which follow the corresponding colored trajectories, the red arrows the polarizations of the $+1/2$ defects, and the pink cross at the origin denotes the apex. Bottom row: corresponding plots on a 3D cone.

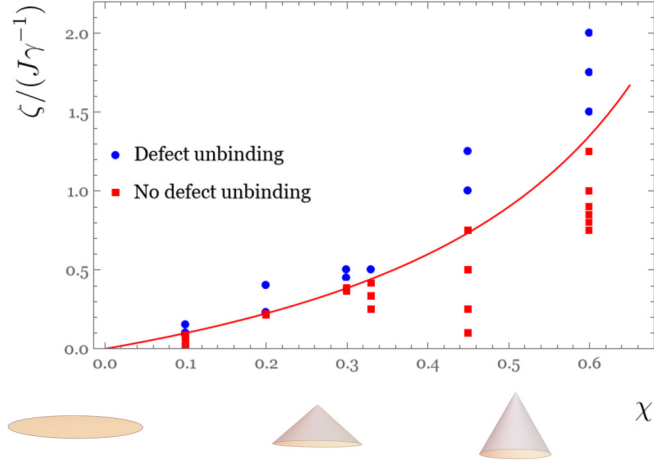


FIG. 11. Plot of data from simulations for when defect unbinding occurs. Red curve corresponds to the analytical prediction [Eq. (30) with a fitting parameter $c' = 0.9$]. The bottom three images are perspective views of a disk and two cones at the corresponding values of χ .

on the flank. See Table V for our simulation results for $\chi = 1/3$, $\frac{\zeta}{J\gamma^{-1}} = .5$, and $\psi = 0, \pi/4$. For $\psi = 0, \pi/4$, we do not have an argument for the stable two-defect orbit observed in our simulations. One possible explanation for the case of $\psi = \pi/4$ is that the observed defect polarizations rotate to point outwards, counteracting the attraction to the cone due to the deficit angle. These results are another indication that as χ and ζ increase, the multidefect ansatz becomes worse. As with the case of single-defect orbit on a cone with $\chi = 1/3$, the simulations reveal that for $\psi = \pi/4$ the polarizations of the defects rotated to point outwards. The global phase ψ may in fact become space-dependent as χ and ζ increase, which is not captured in our ansatz.

B. Apex-mediated defect nucleation and emission

Increasing both the activity ζ and the cone deficit angle $2\pi\chi$ reveals an intriguing mechanism for a $2 \rightarrow 1$ defect transition. For sufficiently large χ and activity, a $\pm 1/2$ defect pair is first nucleated at the apex, and then the $-1/2$ defect leaves the apex and annihilates one of the two $+1/2$ flank defects, leaving behind one $+1/2$ defect at the apex and the other $+1/2$ defect on the flanks. See Fig. 5 for phase diagram from simulations, and Fig. 12 depicting key snapshots of this mechanism for $\psi = \pi/4$.

The idea is that to unbind, two conditions need to be met:

TABLE V. Table of defect distances from the cone apex in isothermal coordinates for $\chi = 1/3$ and $\zeta/(J\gamma^{-1}) = .5$ for $\psi = 0, \pi/4$, as determined by simulations on a cone. Here $a = 0.9$. We do not have a theoretical prediction here since activity is large.

Phase ψ	Numerical distance
0	0.93R
$\pi/4$	0.86R

(1) nucleation: the defect pair needs to be created, followed by

(2) emission: a $-1/2$ defect needs to be able to leave the apex.

For condition 1, even though we do not know how to quantify when this occurs, we would expect that the larger the activity, and the larger the curvature at the apex, i.e., the greater the χ . However, condition 2 is easier to quantify, and yields a lower bound on χ for the unbinding to occur, as we now explain. Suppose a $\pm 1/2$ defect pair nucleates at the apex, where the defects are separated by the smallest distance a such that the defects are discernible. Then in order for the $-1/2$ defect to unbind from the $+1/2$ defect at the apex, the net force on the $-1/2$ defect should be repulsive. Since from Eq. (15) the net force F on the $\sigma = -1/2$ defect on the positive real axis is

$$\begin{aligned} F &= 2\pi J \left[-\chi \left(\sigma - \frac{1}{2} \sigma^2 \right) - \sigma^2 \right] / a \\ &= 2\pi J \left[-\chi \left(-\frac{1}{2} - \frac{1}{2} \left(-\frac{1}{2} \right)^2 \right) - \frac{1}{4} \right] / a, \end{aligned} \quad (31)$$

the critical $\chi = \chi_c$ is obtained by setting $F = 0$, leading to $\chi_c = 2/5$, where for $\chi > \chi_c$ the force $F > 0$ and is repulsive. This prediction is consistent with the dashed pink curve in Fig. 5, i.e., that there is no defect nucleation for $\chi < 0.4$. However, our simulations (Fig. 5) indicate that χ_c also depends on the activity. Indeed, we see that for sufficiently large activity, i.e., when one expects condition 1 to be met, then the numerical value of χ_c obtained from simulations is approximately 0.4. For lower activity, however, to create a defect pair, we would expect that a larger χ is needed, which is indeed consistent with what we see in our simulations, as indicated by the dashed pink curve which slants to the right in Fig. 5.

C. Stable cyclic apex-mediated defect pair nucleation, emission, and unbinding

Finally, our simulations reveal that further increase in activity and deficit angle results in exotic cyclic defect pair nucleation, emission, and unbinding, which may be chaotic in time. See Fig. 13 for key snapshots depicting this remarkable behavior for $\psi = \pi/4$. Some qualitative insights into this behavior follow: previously, we have seen that for sufficiently large deficit angle $2\pi\chi$, defect nucleation and emission can occur, causing a transition from a two-defect orbit to a stable one defect orbit, i.e., a $2 \rightarrow 1$ defect transition. However, we have also seen that for sufficiently large activity ζ , a single-defect orbit can become a stable circular two-defect orbit by defect unbinding from the apex, i.e., a $1 \rightarrow 2$ defect transition. It thus seems plausible that for sufficiently large χ and ζ , both of these transitions could happen successively. A more complete phase diagram as a function of activity and cone deficit angle based on our simulation results is provided in Fig. 5, where we summarize the main dynamical states and transitions between them explained in this paper.

VIII. DISCUSSION

In this work, we have investigated the dynamics of a compressible, overdamped active nematic on disks and cones,

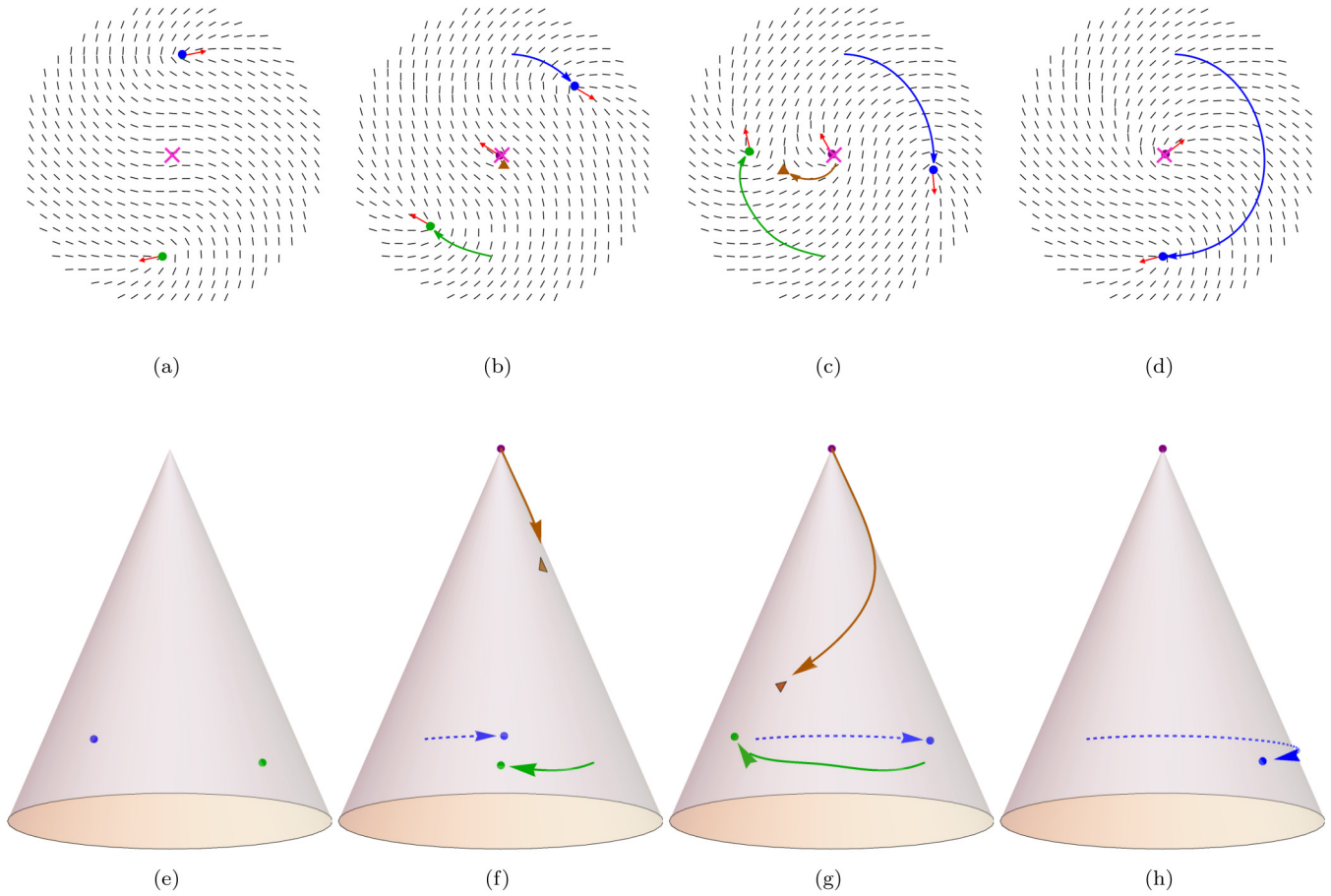


FIG. 12. Key snapshots of simulations depicting the mechanism of defect nucleation at the apex followed by a $-1/2$ defect targeting and annihilating an orbiting $+1/2$ defect. Top row: plots are in isothermal coordinates on a cone with $\chi = 0.6$ and $\zeta/(J\gamma^{-1}) = 1.25$ and $\psi = \pi/4$. (a) Initially two $+1/2$ defects are orbiting. (b) a neutral defect pair is nucleated at the apex. (c) the $-1/2$ defect is emitted from the apex and targets one of the orbiting $+1/2$ defects (d) the $-1/2$ defect has successfully annihilated one of the orbiting $+1/2$ defects, and the other orbiting $+1/2$ defect continues to orbit. In all of the plots, the colored dots denote the $+1/2$ defects, the orange triangle denotes the $-1/2$ defect, defects follow the corresponding colored trajectories, the red arrows the polarizations of the $+1/2$ defects, and the pink cross at the origin denotes the apex. Bottom row: corresponding plots on a 3D cone, where dashed lines indicate defect trajectories on the far side of the cone.

with a focus on the role of boundary conditions. By imposing strong anchoring boundary conditions at the base of a disk or a cone, we have uncovered a rich phase diagram of circular orbits of one or two $+1/2$ flank defects, with transitions between these ordered dynamical states mediated by defect absorption, defect unbinding, and defect pair nucleation at the apex. Strong anchoring boundary conditions with the director at a 45° angle to the cone base are particularly interesting. Moreover, the Born-Oppenheimer approximation (nematic textures instantaneously follow defect positions) allows us to make analytical predictions about the dynamics of active nematic defects on curved geometries. Many of these predictions were indeed corroborated by our full numerical simulations. For example, balancing the Coulomb forces (including those from image charges) with the motile active force led to stable circular orbits in the regime of low activity and deficit angle, at locations predicted by the theory. And at higher activity, the prediction for the critical activity for defect unbinding from the apex agreed with theory. Going beyond what can be derived from a simple Born-Oppenheimer approximation, the full numerical simulations revealed that curvature, acting

as a lightning rod with activity serving as the catalyst, can induce the nucleation of neutral defect pairs, with the emission of mobile $-1/2$ defects, despite their local 3-fold symmetry. This finding provides a route and possible explanation for defect pair nucleation in more general curved active systems.

It is natural to ask how our results for defect absorption and emission at the cone apex depend on the sharpness of the lighting-rod-like tip structures studied here. Because of the topological nature of the geometrical frustration associated with the cone, which reveals itself in parallel transport of order parameters even far away from the apex, we expect that cones with truncated tips would behave in a similar fashion, provided the radius of the truncated tip is small compared to the overall cone size and, furthermore, provided we keep the same boundary conditions at the base and impose free boundary conditions along the rim of the truncated tip. Free boundary conditions at the rim allow easy creation and destruction of defects onto the cone flanks via image defects. Similar expectations for defect ground states with tangential boundary conditions in the absence of activity were tested in Ref. [50].

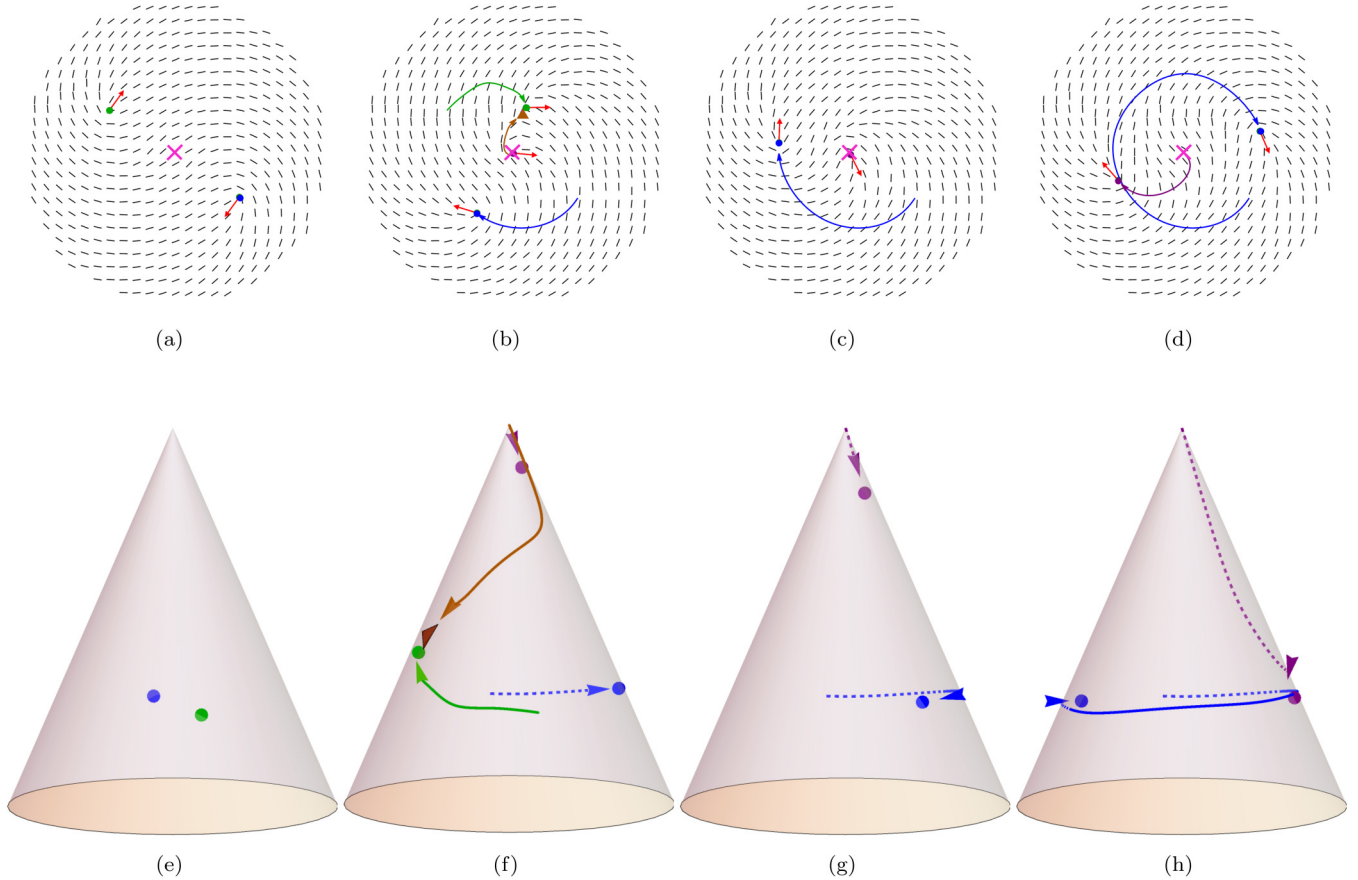


FIG. 13. Key snapshots of simulations depicting cyclic $2 \rightarrow 1 \rightarrow 2 \dots$ defect transition mechanism. Top row: plots are in isothermal coordinates on a cone with $\chi = 0.6$ and $\zeta/(J\gamma^{-1}) = 2$ and $\psi = \pi/4$. (a) Initially two $+1/2$ defects are orbiting. (b) a neutral defect pair is nucleated at the apex and then the $-1/2$ defect is emitted from the apex and targets one of the orbiting $+1/2$ defects (c) the $-1/2$ defect has successfully annihilated one of the orbiting $+1/2$ defects, and the other orbiting $+1/2$ defect continues to orbit. (d) the $+1/2$ defect has successfully unbound (escaped) from the apex. In all of the plots, the colored dots denote the $+1/2$ defects, the orange triangle the $-1/2$ defect, defects follow the corresponding colored trajectories, the red arrows the polarizations of the $+1/2$ defects, and the pink cross at the origin denotes the apex. Bottom row: corresponding plots on a 3D cone, where dashed lines indicate defect trajectories on the far side of the cone.

We now comment on the relation of our work to other interesting investigations [23,29,32], which considered the related model of an incompressible nematic on a disk or an annulus. Although there is no geometric charge at the center, as occurs at the apex for cones with $\chi > 0$, Ref. [32] via simulations found that for sufficiently large activity, a two-defect orbit with tangential boundary conditions can become stable via defect pair nucleation at the origin followed by defect emission of the $-1/2$ defect which then annihilates one of the original orbiting $+1/2$ defects, similar to the mechanism discussed in Sec. VII B. Experiments on a disk in Ref. [23] show that $2 \rightarrow 1 \rightarrow 2 \dots$ transitions occur via defect pair nucleation at the boundary followed by annihilation and then again defect pair nucleation, etc, similar to our mechanism in Sec. VII C, with the intriguing difference that defect pair nucleation occurs at the boundary vs the apex for our case. Finally, Ref. [29] numerically found a phase diagram in the case of a disk and annulus, which when restricted to the regime where the inner radius of the annulus is small compared to the outer radius, agrees with our phase diagram (Fig. 5) for small deficit angle: for small activity, circular orbits are allowed, and for large activity, the dynamics is chaotic. The results of

this specific annulus geometry is not surprising since it is akin to a truncated cone, with free boundary conditions imposed at the truncation [50]. An inverted truncated cone is like a banked racetrack, and it would be interesting to study active nematic dynamics on such a structure as a function of apex ratio, with an unquantized Gaussian curvature residing inside the truncation.

In the future, it would be worth studying the dynamics of active matter coating a *hyperbolic* cone. Preliminary investigations of ground states have revealed that even in the passive setting, extra neutral defect pairs leading to additional $+1/2$ flank defects are nucleated at the apex, depending on the deficit angle [69]. It would also be worth exploring further the regime of large activity, where we expect active turbulence, interacting with a delta function of Gaussian curvature, leading to an active analog of the Debye-Hückel screening problem of electrolytes in two dimensions.

Finally, it is worth noting the possible experimental setups that could test our theoretical and computational predictions. It has already been demonstrated that by using a rotating cuvette containing a yield-stress fluid, one can form toroidal droplets on which mixtures of microtubule-kinesin

motor mixtures are stabilized and nucleate active nematic topological defects [45]. Extending this elegant experimental technique to stabilize active nematic microtubule-motor protein mixtures on conical droplets might be challenging, but could be an ideal test case for exploring active defect dynamics in a controlled manner. By tuning the sharpness of the cone in yield-stress droplets of various shapes, and the activity through varying ATP concentration, one could probe the phase diagram presented in Fig. 1. Similarly, the possibility of forming cell monolayers on corrugated surfaces has been demonstrated using polyacrylamide hydrogels fabrication by UV photocrosslinking [70]. This technique can be easily adapted to achieve cell monolayers on conical surfaces of varying sharpness. We expect especially complex dynamics when χ moves closer to 1 and the activity becomes large. One could then probe dynamics of elongated, weakly adhesive mesenchymal cells such as mouse fibroblast to explore the rich phase diagram studied here. Indeed, such cell layers were already instrumental to probe defect locations in confined disks [30]. Confining defects to the cone, together with our theoretical and computational predictions, could result in one of the first quantitative assessments of topological defect unbinding in active matter with a controlled environment. In addition to subcellular filaments and cell layers, important examples of living liquid crystals, embedding active bacteria in pre-patterned liquid crystal textures [71] could be a fertile

ground for testing active nematic defects on cones as examples of nontrivial curvature singularities. Indeed, such living liquid crystals have been shown to exhibit active nematic defects [72], and the possibility of forming passive liquid crystals on conical geometries has been demonstrated [73]. As such, living liquid crystals on a cone could provide another controlled means for obtaining dynamically ordered defect structures and studying details of defect emission, nucleation, and unbinding in active matter, as explored in this paper.

ACKNOWLEDGMENTS

This work is partially supported by the Center for Mathematical Sciences and Applications at Harvard University (F.V.), and by the Harvard Materials Research Science and Engineering Center via Grant DMR-2011754 (D.R.N.). A.D. acknowledges funding from the Novo Nordisk Foundation (Grant No. NNF18SA0035142 and NERD Grant No. NNF21OC0068687), Villum Fonden (Grant No. 29476), and the European Union (ERC, PhysCoMeT, Grant No. 101041418). Views and opinions expressed are, however, those of the authors only and do not necessarily reflect those of the European Union or the European Research Council. Neither the European Union nor the granting authority can be held responsible for them.

-
- [1] T. Sanchez, D. T. N. Chen, S. J. DeCamp, M. Heymann, and Z. Dogic, Spontaneous motion in hierarchically assembled active matter, *Nature (London)* **491**, 431 (2012).
 - [2] F. C. Keber, E. Loiseau, T. Sanchez, S. J. DeCamp, L. Giomi, M. J. Bowick, M. C. Marchetti, Z. Dogic, and A. R. Bausch, Topology and dynamics of active nematic vesicles, *Science* **345**, 1135 (2014).
 - [3] R. Zhang, N. Kumar, J. L. Ross, M. L. Gardel, and J. J. De Pablo, Interplay of structure, elasticity, and dynamics in actin-based nematic materials, *Proc. Natl. Acad. Sci. USA* **115**, E124 (2018).
 - [4] D. Dell'Arciprete, M. Blow, A. Brown, F. Farrell, J. S. Lintuvuori, A. McVey, D. Marenduzzo, and W. C. Poon, A growing bacterial colony in two dimensions as an active nematic, *Nat. Commun.* **9**, 4190 (2018).
 - [5] Z. You, D. J. G. Pearce, A. Sengupta, and L. Giomi, Geometry and mechanics of microdomains in growing bacterial colonies, *Phys. Rev. X* **8**, 031065 (2018).
 - [6] K. Copenhagen, R. Alert, N. S. Wingreen, and J. W. Shaevitz, Topological defects promote layer formation in *Myxococcus xanthus* colonies, *Nat. Phys.* **17**, 211 (2021).
 - [7] G. Duclos, C. Blanch-Mercader, V. Yashunsky, G. Salbreux, J.-F. Joanny, J. Prost, and P. Silberzan, Spontaneous shear flow in confined cellular nematics, *Nat. Phys.* **14**, 728 (2018).
 - [8] C. Blanch-Mercader, V. Yashunsky, S. Garcia, G. Duclos, L. Giomi, and P. Silberzan, Turbulent dynamics of epithelial cell cultures, *Phys. Rev. Lett.* **120**, 208101 (2018).
 - [9] P. G. de Gennes and J. Prost, *The Physics of Liquid Crystals* (Clarendon Press, Oxford, UK, 1993).
 - [10] D. Needleman and Z. Dogic, Active matter at the interface between materials science and cell biology, *Nat. Rev. Mater.* **2**, 17048 (2017).
 - [11] A. Doostmohammadi, J. Ignés-Mullol, J. M. Yeomans, and F. Sagués, Active nematics, *Nat. Commun.* **9**, 3246 (2018).
 - [12] S. Shankar, A. Souslov, M. J. Bowick, M. C. Marchetti, and V. Vitelli, Topological active matter, *Nat. Rev. Phys.* **4**, 380 (2022).
 - [13] T. B. Saw, A. Doostmohammadi, V. Nier, L. Kocgozlu, S. Thampi, Y. Toyama, P. Marcq, C. T. Lim, J. M. Yeomans, and B. Ladoux, Topological defects in epithelia govern cell death and extrusion, *Nature (London)* **544**, 212 (2017).
 - [14] K. Kawaguchi, R. Kageyama, and M. Sano, Topological defects control collective dynamics in neural progenitor cell cultures, *Nature (London)* **545**, 327 (2017).
 - [15] O. J. Meacock, A. Doostmohammadi, K. R. Foster, J. M. Yeomans, and W. M. Durham, Bacteria solve the problem of crowding by moving slowly, *Nat. Phys.* **17**, 205 (2021).
 - [16] Y. Maroudas-Sacks, L. Garion, L. Shani-Zerbib, A. Livshits, E. Braun, and K. Keren, Topological defects in the nematic order of actin fibres as organization centres of hydra morphogenesis, *Nat. Phys.* **17**, 251 (2021).
 - [17] A. Doostmohammadi and B. Ladoux, Physics of liquid crystals in cell biology, *Trends Cell Biol.* **32**, 140 (2022).
 - [18] M. J. Bowick, N. Fakhri, M. C. Marchetti, and S. Ramaswamy, Symmetry, thermodynamics, and topology in active matter, *Phys. Rev. X* **12**, 010501 (2022).
 - [19] S. Shankar, L. V. D. Scharrer, M. J. Bowick, and M. C. Marchetti, Design rules for controlling active topological defects, *Proc. Natl. Acad. Sci. USA* **121**, e2400933121 (2024).

- [20] R. Zhang, A. Mozaffari, and J. J. de Pablo, Autonomous materials systems from active liquid crystals, *Nat. Rev. Mater.* **6**, 437 (2021).
- [21] T. N. Shendruk, A. Doostmohammadi, K. Thijssen, and J. M. Yeomans, Dancing disclinations in confined active nematics, *Soft Matter* **13**, 3853 (2017).
- [22] J. Hardoüin, R. Hughes, A. Doostmohammadi, J. Laurent, T. Lopez-Leon, J. M. Yeomans, J. Ignés-Mullol, and F. Sagués, Reconfigurable flows and defect landscape of confined active nematics, *Commun. Phys.* **2**, 121 (2019).
- [23] A. Opathalage, M. M. Norton, M. P. Juniper, B. Langeslay, S. A. Aghvami, S. Fraden, and Z. Dogic, Self-organized dynamics and the transition to turbulence of confined active nematics, *Proc. Natl. Acad. Sci. USA* **116**, 4788 (2019).
- [24] S. Chandragiri, A. Doostmohammadi, J. M. Yeomans, and S. P. Thampi, Active transport in a channel: Stabilisation by flow or thermodynamics, *Soft Matter* **15**, 1597 (2019).
- [25] M. Varghese, A. Baskaran, M. F. Hagan, and A. Baskaran, Confinement-induced self-pumping in 3D active fluids, *Phys. Rev. Lett.* **125**, 268003 (2020).
- [26] S. Chandragiri, A. Doostmohammadi, J. M. Yeomans, and S. P. Thampi, Flow states and transitions of an active nematic in a three-dimensional channel, *Phys. Rev. Lett.* **125**, 148002 (2020).
- [27] Z.-Y. Li, D.-Q. Zhang, and B. Li, Formation and propagation of solitonlike defect clusters in confined active nematics with chiral anchoring, *Phys. Rev. Res.* **3**, 023253 (2021).
- [28] C. G. Wagner, M. M. Norton, J. S. Park, and P. Grover, Exact coherent structures and phase space geometry of preturbulent 2D active nematic channel flow, *Phys. Rev. Lett.* **128**, 028003 (2022).
- [29] C. Joshi, Z. Zarei, M. Norton, S. Fraden, A. Baskaran, and M. F. Hagan, From disks to channels: Dynamics of active nematics confined to an annulus, *Soft Matter* **19**, 5630 (2023).
- [30] G. Duclos, C. Erlenkämper, J.-F. Joanny, and P. Silberzan, Topological defects in confined populations of spindle-shaped cells, *Nat. Phys.* **13**, 58 (2017).
- [31] T. Gao, M. D. Betterton, A.-S. Jhang, and M. J. Shelley, Analytical structure, dynamics, and coarse graining of a kinetic model of an active fluid, *Phys. Rev. Fluids* **2**, 093302 (2017).
- [32] M. M. Norton, A. Baskaran, A. Opathalage, B. Langeslay, S. Fraden, A. Baskaran, and M. F. Hagan, Insensitivity of active nematic liquid crystal dynamics to topological constraints, *Phys. Rev. E* **97**, 012702 (2018).
- [33] L. Mirantsev, Behavior of chiral active nematics confined to nanoscopic circular region, *Eur. Phys. J. E* **44**, 112 (2021).
- [34] J. Hardoüin, C. Doré, J. Laurent, T. Lopez-Leon, J. Ignés-Mullol, and F. Sagués, Active boundary layers in confined active nematics, *Nat. Commun.* **13**, 6675 (2022).
- [35] A. Sciortino, L. J. Neumann, T. Krüger, I. Maryshev, T. F. Teshima, B. Wolfrum, E. Frey, and A. R. Bausch, Polarity and chirality control of an active fluid by passive nematic defects, *Nat. Mater.* **22**, 260 (2023).
- [36] K.-T. Wu, J. B. Hishamunda, D. T. Chen, S. J. DeCamp, Y.-W. Chang, A. Fernández-Nieves, S. Fraden, and Z. Dogic, Transition from turbulent to coherent flows in confined three-dimensional active fluids, *Science* **355**, eaal1979 (2017).
- [37] S. Chen, P. Gao, and T. Gao, Dynamics and structure of an apolar active suspension in an annulus, *J. Fluid Mech.* **835**, 393 (2018).
- [38] J. Hardoüin, J. Laurent, T. Lopez-Leon, J. Ignés-Mullol, and F. Sagués, Active microfluidic transport in two-dimensional handlebodies, *Soft Matter* **16**, 9230 (2020).
- [39] E. de Oliveira, L. Mirantsev, M. Lyra, and I. de Oliveira, Orientational ordering of active nematics confined to a 2D nanoscopic ring-shaped cavity, *J. Mol. Liq.* **377**, 121513 (2023).
- [40] T. C. Lubensky and J. Prost, Orientational order and vesicle shape, *J. Phys. II France* **2**, 371 (1992).
- [41] R. Zhang, Y. Zhou, M. Rahimi, and J. J. De Pablo, Dynamic structure of active nematic shells, *Nat. Commun.* **7**, 13483 (2016).
- [42] F. Alaimo, C. Köhler, and A. Voigt, Curvature controlled defect dynamics in topological active nematics, *Sci. Rep.* **7**, 5211 (2017).
- [43] M. Clairand, A. Mozaffari, J. Hardoüin, R. Zhang, C. Doré, J. Ignés-Mullol, F. Sagués, J. J. de Pablo, and T. Lopez-Leon, Dynamics of active defects on the anisotropic surface of an ellipsoidal droplet, [arXiv:2303.13312](https://arxiv.org/abs/2303.13312).
- [44] M. Bowick, D. R. Nelson, and A. Travesset, Curvature-induced defect unbinding in toroidal geometries, *Phys. Rev. E* **69**, 041102 (2004).
- [45] P. W. Ellis, D. J. Pearce, Y.-W. Chang, G. Goldsztein, L. Giomi, and A. Fernandez-Nieves, Curvature-induced defect unbinding and dynamics in active nematic toroids, *Nat. Phys.* **14**, 85 (2018).
- [46] V. Vitelli and A. M. Turner, Anomalous coupling between topological defects and curvature, *Phys. Rev. Lett.* **93**, 215301 (2004).
- [47] G. H. Zhang and D. R. Nelson, Fractional defect charges in liquid crystals with p -fold rotational symmetry on cones, *Phys. Rev. E* **105**, 054703 (2022).
- [48] F. Vafa, D. R. Nelson, and A. Doostmohammadi, Active topological defect absorption by a curvature singularity, *J. Phys.: Condens. Matter* **35**, 425101 (2023).
- [49] F. Vafa and L. Mahadevan, Statics and diffusive dynamics of surfaces driven by p -atic topological defects, *Soft Matter* **19**, 6652 (2023).
- [50] F. Vafa, G. H. Zhang, and D. R. Nelson, Defect absorption and emission for p -atic liquid crystals on cones, *Phys. Rev. E* **106**, 024704 (2022).
- [51] F. Vafa and L. Mahadevan, Active nematic defects and epithelial morphogenesis, *Phys. Rev. Lett.* **129**, 098102 (2022).
- [52] C. F. Gauss, On conformal representations, in *A Source Book in Mathematics*, edited by D. E. Smith (Dover, Mineola, NY, 1959), pp. 463–475.
- [53] F. C. Frank, I. Liquid crystals: On the theory of liquid crystals, *Discuss. Faraday Soc.* **25**, 19 (1958).
- [54] D. W. Berreman and S. Meiboom, Tensor representation of Oseen-Frank strain energy in uniaxial cholesterics, *Phys. Rev. A* **30**, 1955 (1984).
- [55] F. Vafa, M. J. Bowick, M. C. Marchetti, and B. I. Shraiman, Multi-defect dynamics in active nematics (2020), [arXiv:2007.02947](https://arxiv.org/abs/2007.02947).
- [56] A. J. Vromans and L. Giomi, Orientational properties of nematic disclinations, *Soft Matter* **12**, 6490 (2016).
- [57] One can instead consider antitwist boundary conditions, by which we mean that the nematic director rotates clock-wise around a counter-clockwise loop on the boundary. The net topological charge is thus -1 , which means that in the ground state on a disk, there will be two antipodal $-1/2$ defects, just as in

- the case of tangential boundary conditions for $+1/2$ defects. Unlike $+1/2$ defects, since $-1/2$ defects are not motile, we do not expect the introduction of activity to cause the $-1/2$ defects to orbit, which we checked numerically for small activity. It might be interesting to study this problem for large activity.
- [58] L. Bonn, A. Ardaševa, R. Mueller, T. N. Shendruk, and A. Doostmohammadi, Fluctuation-induced dynamics of nematic topological defects, *Phys. Rev. E* **106**, 044706 (2022).
- [59] A. Doostmohammadi, M. F. Adamer, S. P. Thampi, and J. M. Yeomans, Stabilization of active matter by flow-vortex lattices and defect ordering, *Nat. Commun.* **7**, 10557 (2016).
- [60] E. Putzig, G. S. Redner, A. Baskaran, and A. Baskaran, Instabilities, defects, and defect ordering in an overdamped active nematic, *Soft Matter* **12**, 3854 (2016).
- [61] P. Srivastava, P. Mishra, and M. C. Marchetti, Negative stiffness and modulated states in active nematics, *Soft Matter* **12**, 8214 (2016).
- [62] A. U. Oza and J. Dunkel, Antipolar ordering of topological defects in active liquid crystals, *New J. Phys.* **18**, 093006 (2016).
- [63] L. Landau and E. Lifshitz, *Quantum Mechanics: Non-Relativistic Theory*, 3rd ed., Course of Theoretical Physics (Elsevier Science, Amsterdam, 2013).
- [64] F. Vafa, Defect dynamics in active polar fluids vs. active nematics, *Soft Matter* **18**, 8087 (2022).
- [65] W. E. Schiesser, *The Numerical Method of Lines: Integration of Partial Differential Equations* (Elsevier, Amsterdam, 2012).
- [66] W. Press, B. Flannery, S. Teukolsky, and W. Vetterling, Multistep, multivalued, and predictor-corrector methods, in *Numerical Recipes in FORTRAN: The Art of Scientific Computing* (Cambridge University Press, Cambridge, UK, 1992), p. 740.
- [67] J. Dzubiella, M. Schmidt, and H. Löwen, Topological defects in nematic droplets of hard spherocylinders, *Phys. Rev. E* **62**, 5081 (2000).
- [68] J. Galanis, D. Harries, D. L. Sackett, W. Losert, and R. Nossal, Spontaneous patterning of confined granular rods, *Phys. Rev. Lett.* **96**, 028002 (2006).
- [69] F. Vafa, G. H. Zhang, and D. R. Nelson, Defect ground states for liquid crystals on cones and hyperbolic cones, [arXiv:2405.03742](https://arxiv.org/abs/2405.03742).
- [70] M. Luciano, S.-L. Xue, W. H. De Vos, L. Redondo-Morata, M. Surin, F. Lafont, E. Hannezo, and S. Gabriele, Cell monolayers sense curvature by exploiting active mechanics and nuclear mechanoadaptation, *Nat. Phys.* **17**, 1382 (2021).
- [71] T. Turiv, R. Koizumi, K. Thijssen, M. M. Genkin, H. Yu, C. Peng, Q.-H. Wei, J. M. Yeomans, I. S. Aranson, A. Doostmohammadi *et al.*, Polar jets of swimming bacteria condensed by a patterned liquid crystal, *Nat. Phys.* **16**, 481 (2020).
- [72] S. Zhou, A. Sokolov, O. D. Lavrentovich, and I. S. Aranson, Living liquid crystals, *Biophys. J.* **106**, 420a (2014).
- [73] J. Lagerwall, Liquid crystal elastomer actuators and sensors: Glimpses of the past, the present and perhaps the future, *Program. Mater.* **1**, e9 (2023).